Front. Earth Sci. 2023, 17(1): 322–336
https://doi.org/10.1007/s11707-021-0966-5

RESEARCH ARTICLE

Gas in place and its controlling factors of deep shale of the Wufeng–Longmaxi Formations in the Dingshan area, Sichuan Basin

Ping GAO[1], Xianming XIAO (✉)[1], Dongfeng HU[2], Ruobing LIU[2], Fei LI[2], Qin ZHOU[3], Yidong CAI[1], Tao YUAN[2], Guangming MENG[1]

1 School of Energy Resources, China University of Geosciences (Beijing), Beijing 100083, China
2 Sinopec Exploration Branch Company, Chengdu 610041, China
3 State Key Laboratory of Organic Geochemistry, Guangzhou Institute of Geochemistry, Chinese Academy of Sciences, Guangzhou 510640, China

© Higher Education Press 2022

Abstract Recently, deeply-buried shale (depth > 3500 m) has become an attractive target for shale gas exploration and development in China. Gas-in-place (GIP) is critical to shale gas evaluation, but the GIP content of deep shale and its controlling factors have rarely been investigated. To clarify this issue, an integrated investigation of deep gas shale (3740–3820 m depth) of the Lower Paleozoic Wufeng–Longmaxi Formations (WF–LMX) in the Dingshan area, Sichuan Basin had been carried out. Our results show that the GIP content of the studied WF–LMX shale in the Dingshan area ranges from 0.85 to 12.7 m^3/t, with an average of 3.5 m^3/t. Various types of pores, including organic matter (OM) pore and inorganic pore, are widely developed in the deep shale, with total porosity of 2.2 to 7.3% (average = 4.5%). The OM pore and clay-hosted pore are the dominant pore types of siliceous shale and clay-rich shale, respectively. Authigenic quartz plays a critical role in the protection of organic pores in organic-rich shales from compaction. The TOC content controls the porosity of shale samples, which is the major factor controlling the GIP content of the deep shale. Clay minerals generally play a negative role in the GIP content. In the Sichuan Basin, the deep and ultra-deep WF–LMX shales display the relatively high porosity and GIP contents probably due to the widespread of organic pores and better preservation, revealing great potentials of deep and ultra-deep shale gas. From the perspective of rock mechanical properties, deep shale is the favorable exploration target in the Sichuan Basin at present. However, ultra-deep shale is also a potential exploration target although there remain great challenges.

Received December 15, 2021; accepted January 4, 2022

E-mail: xmxiao@cugb.edu.cn

Keywords Deep shale, porosity, organic pore, gas potential, authigenic quartz

1 Introduction

Shale gas has been commercially produced in several countries and regions (e.g., North America and China) over the last decade (Jarvie et al., 2007; Bustin et al., 2009; Jarvie, 2012; Loucks et al., 2012; Hao et al., 2013; Dong et al., 2014; Nie et al., 2019a, 2019b, 2021; Chen et al., 2021), and the burial depth of major producing layers in shale gas fields rarely exceeds 3500 m (Jarvie et al., 2007; Jarvie, 2012; Milliken et al., 2013; Kosanke et al., 2019). According to the current technology level of shale gas exploitation, gas shale reservoirs with burial depth greater than 3500 m can be divided into two categories: deep shale (3500–4500 m) and ultra-deep shale (4500–6000 m) (Long et al., 2018; He et al., 2020; Guo, 2021; Ma et al., 2021). Exploration activities of deep shale gas were first conducted in the United States (Abou-Sayed et al., 2011; Wood et al., 2011; Farinas and Fonseca, 2013), and several deep shale gas fields, e.g., Haynesville, Eagle Ford, Cana Woodford, Hilliard-Baxter-Mancos, and Mancos, had been discovered (Jarvie, 2012; Farinas and Fonseca, 2013). Among them, the former three have been commercially exploited since 2007, the gas yield of single well can be up to 5×10^4 m^3/d, and the average of ultimate gas yield of single well exceeds 1×10^8 m^3 (Wood et al., 2011; Chen and Zeng, 2016). According to the US Energy Information Administration (EIA), cumulative gas yield of the Haynesville deep shale gas fields is 806×10^8 m^3 until the October 2020. Moreover, the proportion of deep shale gas yield to

total shale gas yield gradually increased from 13.8% in 2014 to 23.5% in 2020 (Shen et al., 2021).

The exploration and development of shale gas in China have been greatly promoted by the "US shale revolution", and a major breakthrough has been made in the shale of the Lower Paleozoic Wufeng–Longmaxi Formations (WF–LMX) in the Sichuan Basin and adjacent areas (Hao et al., 2013; Guo, 2014; Guo and Zhang, 2014; He et al., 2019b; Lu et al., 2021; Nie et al., 2021). Until the end of 2019, cumulative proved geological reserves of the WF–LMX shale gas had exceeded 1.8 × 10^{12} m^3, and cumulative gas yield had exceeded 300 × 10^8 m^3 (Qiu and Zou, 2020). However, commercial exploitation of the WF–LMX shale gas has largely focused in mid-shallow depths (< 3500 m), and three major shale gas fields, i.e., Fuling (or Jiaoshiba), Weiyuan, and Changning-Zhaotong Shale Gas Fields, has been established (Fig. 1; Hao et al., 2013; Guo and Zhang, 2014; He et al., 2019b; Nie et al., 2021). It has been estimated that the area and geological reserves of the WF–LMX deep shale (> 3500 m depth) in the Sichuan Basin were twice of those of mid-shallow shale (Long et al., 2018; He et al., 2020), and deep shale gas is becoming a major alternative target for shale gas exploration and development in China (e.g., Long et al., 2018; He et al., 2020; Guo et al., 2020; Guo, 2021; Ma et al., 2021; Gao et al., 2022). Most recently, Chinese oil companies, including PetroChina and Sinopec, have made great attempts on the deep shale gas exploration, and suggest that the WF–LMX deep shale in the southern Sichuan Basin is a favorable exploration target (Long et al., 2018; Ma et al., 2021). For example, the WF–LMX high-quality shale with burial depth of 3662 m in the Well WY1 yielded a gas flow of 17.5 × 10^4 m^3/d after the fracturing of 1600-m horizontal section in the March 2015, and the first deep shale gas field in China had been discovered, i.e., Weiyuan-Rongxian Shale Gas Field (Fig. 1; Guo, 2021; Ma et al., 2021). In the November 2015, the fracturing of 1000-m horizontal section of the WF–LMX shale in the Well YY1, with burial depth of 3890 m, yielded a gas flow of 13.6 × 10^4 m^3/d, and the proved reserves of the Yongchuan Deep Shale Gas Field was estimated to be 234.53 × 10^8 m^3 (Guo, 2021). Deep shale gas exploration in the Dingshan area of the southeast Sichuan Basin was started as early as 2013. A deep shale gas well (DY2) was drilled with a depth of 5700 m, with the burial depth of 4417 m and the length of horizontal section of 1034 m, which yielded a gas flow of 10.52 × 10^4 m^3/d (Guo, 2021). Subsequently, a series of deep

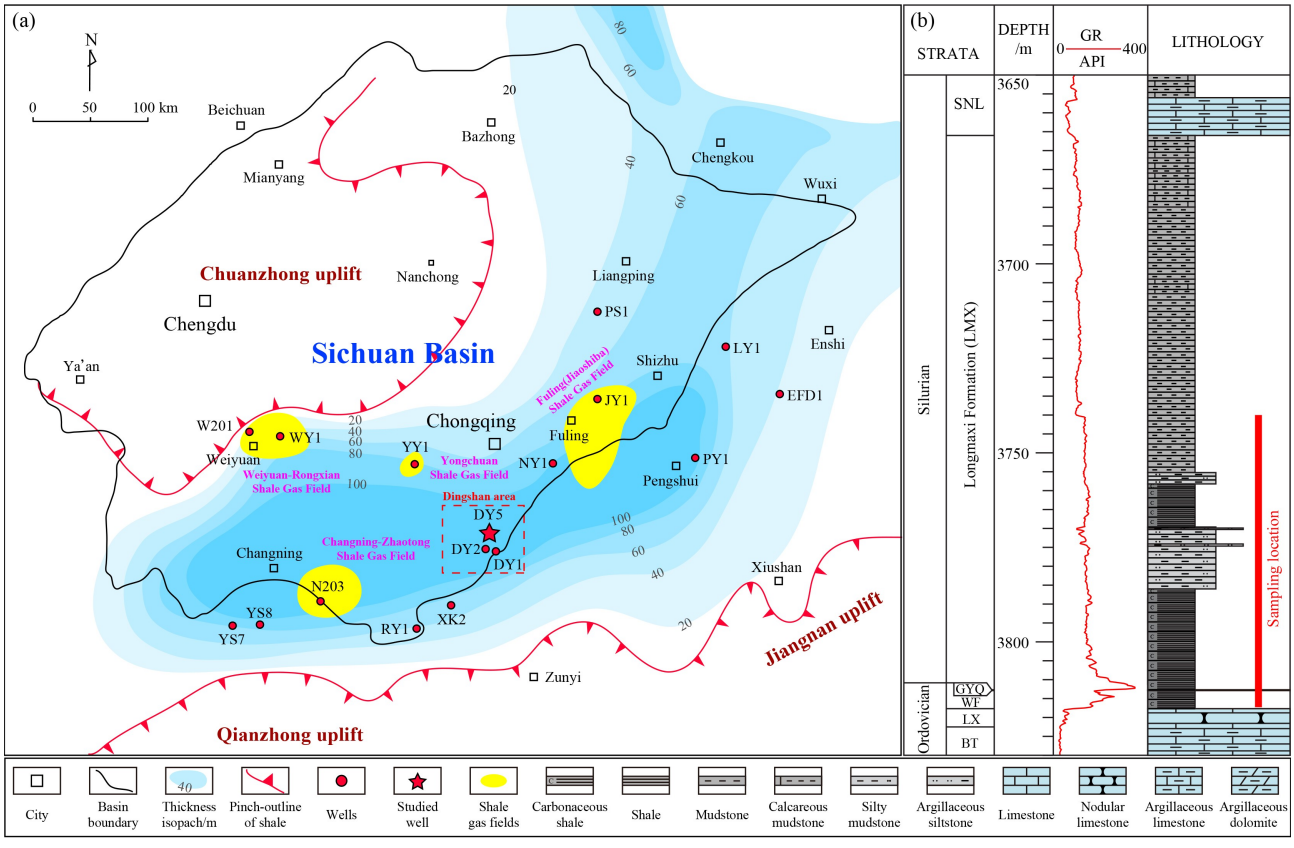

Fig. 1 (a) Distribution and thickness of the Longmaxi Formation shale in the Sichuan Basin and their neighboring areas (modified from Guo and Zhang, 2014), and the location of studied Well DY5; (b) Stratigraphic column for the Upper Ordovician-Lower Silurian of the Well DY5. Notes: SNL = Shiniulan Formation; GYQ = Guanyinqiao Member; WF = Wufeng Formation; LX = Linxiang Formation; BT = Baota Formation.

shale gas wells, e.g., Wells DY4, DY5, and DYS1, were drilled, and yielded commercial gas flows of 20.56 × 10^4 m^3/d, 16.33 × 10^4 m^3/d, and 31.18 × 10^4 m^3/d, respectively (Guo, 2021), thus revealing great potentials of deep shale gas in the Dingshan area.

Gas-in-place (GIP) content is a vital parameter for shale gas evaluation (Jarvie, 2004, 2012; Ambrose et al., 2012; Pan et al., 2016; Long et al., 2018; Qiu and Zou, 2020; Sun et al., 2020, 2021b). The GIP content of top 10 shale gas fields in the North American ranges from 1.42 to 9.91 m^3/t (Jarvie, 2012). Exploration practice shows that the GIP content greater than 2 m^3/t could be used as a criterion for evaluating the enrichment or depletion of the Lower Paleozoic shale gas in the south China (Wang et al., 2012), and the GIP content greater than 3 m^3/t has been used for identifying the "sweet-spot interval" (Qiu and Zou, 2020). The average GIP content of three major mid-shallow shale gas fields, i.e., Fuling, Weiyuan, and Changning-Zhaotong Shale Gas Fields, is all greater than 2 m^3/t (Dong et al., 2014). However, the GIP content of deep shale in the Sichuan Basin is generally higher than that of mid-shallow shale (e.g., Long et al., 2018; He et al., 2020).

The factors controlling the GIP content of mid-shallow shale have been extensively studied (Jarvie, 2004 and 2021; Jarvie et al., 2007; Qiu and Zou, 2020; Sun et al., 2020, 2021b), mainly including geochemical properties of shale (internal factor) and geological conditions (external factor). The internal factors include total organic carbon (TOC), mineral composition, kerogen type and maturity, porosity, pore type and structure, and water content (e.g., Ross and Bustin, 2002; Chalmers and Bustin, 2007; Xiao et al., 2015; Cheng et al., 2017; Sun et al., 2020, 2021a, 2021b). External factors cover burial depth, preservation condition, pressure coefficient, and presence of faults (Dong et al., 2014; Guo, 2014; He et al., 2019b, 2020). However, the GIP contents of deep and ultra-deep shales have rarely been reported, and their controlling factors remains unclear. Therefore, we present results of the GIP content of the WF–LMX deep shale samples recovered from the Well DY5 in Dingshan area, southeast Sichuan Basin, and the major purpose of this paper is to explore major factors controlling the GIP content of deep shale, thus providing a scientific basis for deep and ultra-deep shale gas exploration.

2 Geological setting and studied section

The Sichuan Basin in southwestern China, with a total area of approximately 19 × 10^4 km^2, is tectonically developed on the upper region of the Yangtze Platform (Hao et al., 2013; Guo and Zhang, 2014). During the Late Ordovician and Early Silurian time, the Upper Yangtze Platform had evolved into a restricted shelf basin due to compression driven by Kwangsian movement (Chen et al., 2004), and a siliciclastic-dominated succession was deposited. Meanwhile, the development of several uplifts around the Sichuan Basin, e.g., Chuanzhong uplift, Qianzhong uplift, and Jiangnan uplift, led to a relative rise of sea level in marine areas (Fig. 1). Therefore, thick, organic-rich black shale was generally deposited in the deep shelf facies, while organic-lean siltstone and silty mudstone were deposited in the shallow shelf facies along the margin of the uplifts (Fig. 1; Guo and Zhang, 2014). Two large global transgressions in the Late Ordovician and Early Silurian time led to the deposition of the WF and LMX Formations (Khan et al., 2019).

The studied well (DY5) is located in the southeast Sichuan Basin and the WF–LMX shale is deposited in deep shelf facies (Guo and Zhang, 2014). The WF shale is dominated by black carbonaceous shale, with total thickness of 4.72 m (Fig. 1). The topmost of the WF shale is the Guanyinqiao Member (GYQ) consisting of 31-cm-thick shell-rich argillaceous dolomite, which deposited during a rapid sea-level falling, corresponding to the Hirnantian glaciations (Chen et al., 2004). The overlying LMX shale is mainly composed of black carbonaceous shale and mudstone intercalated with silty mudstone and argillaceous siltstone, with a total thickness of 146.74 m (Fig. 1). The organic-rich shale was usually developed in the lower part of the LMX shale, with total thickness of 28 m, which has a burial depth greater than 3786 m (Fig. 1).

3 Samples and analytical methods

3.1 Samples

A total of 79 WF–LMX shale samples were collected from the Well DY5, with the burial depth of 3740–3820 m (Fig. 1). The detailed information of studied samples is provided in Table 1. All samples were prepared for geochemical and mineralogical analyses by grinding to a 200 mesh size.

3.2 Analytical methods

3.2.1 SEM observation

The shale plugs, cut perpendicular to the bedding, were first mechanically polished and further polished by an argon ion milling system IM4000 in order to obtain a highly smooth surface. Scanning electron microscopy (SEM) observation of the polished samples were conducted on a high-resolution cold field emission scanning electron microscopy (Hitachi S-8000) equipped with an energy dispersive spectrometer (EDS) at the State Key Laboratory of Organic Geochemistry, Guangzhou Institute of Geochemistry, Chinese Academy of Sciences. Imaging were performed at 1.5 kV and a working distance of 3–4 mm under vacuum. The EDS measurement of candidate minerals was conducted under SE mode with a working distance of 15 mm and a voltage of 15 kV.

Table 1 Basic information, TOC content, porosity, mineralogical compositions, gas contents of the studied shale samples from Well DY5

Sample	Depth /m	Strata	Lithology	TOC /%	Porosity /%	Quartz /%	Feldspar /%	Carbonate /%	Pyrite /%	Clay /%	Desorbed gas /($m^3 \cdot t^{-1}$)	Lost gas /($m^3 \cdot t^{-1}$)	GIP /($m^3 \cdot t^{-1}$)
DY5-X-1	3740.19	Longmaxi Formation	Mudstone		NM	27	4.6	16.3	1.6	50.5	0.343	1.06	1.403
DY5-X-2	3741.02	Longmaxi Formation	Mudstone		NM	29.3	4.4	11	ND	55.3		NM	
DY5-X-3	3741.69	Longmaxi Formation	Mudstone	0.57	3.6	29.7	4.5	8.4	ND	57.4	0.345	1.076	1.421
DY5-X-4	3742.99	Longmaxi Formation	Mudstone	NM	3.8	30.8	4.6	10.2	ND	54.4		NM	
DY5-X-5	3743.55	Longmaxi Formation	Mudstone		NM	29.8	4.8	8.7	ND	56.7	0.249	1.09	1.339
DY5-X-6	3744.97	Longmaxi Formation	Mudstone	0.98	NM	30.3	5	8.8	1.5	54.4		NM	
DY5-X-7	3745.97	Longmaxi Formation	Mudstone	NM	3.8	33.3	4.2	14.5	1.8	46.2	0.408	1.285	1.693
DY5-X-8	3747.07	Longmaxi Formation	Mudstone		NM	31.7	5	9.1	ND	54.2		NM	
DY5-X-9	3748.16	Longmaxi Formation	Mudstone	1.07	3.9	32.1	4.8	10.2	2.3	50.6	0.487	1.777	2.264
DY5-X-10	3748.8	Longmaxi Formation	Mudstone		NM	34.4	5.3	5.5	2.4	52.4		NM	
DY5-X-11	3749.55	Longmaxi Formation	Mudstone		NM	31.8	3.9	9	2.1	53.2	0.446	2.158	2.604
DY5-X-12	3750.85	Longmaxi Formation	Mudstone	1.12	3.9	33.6	6	5.4	1.7	53.3		NM	
DY5-X-13	3751.55	Longmaxi Formation	Mudstone		NM	31.6	5	4.6	1.5	57.3	0.417	1.647	2.064
DY5-X-14	3752.84	Longmaxi Formation	Mudstone		NM	35.4	5.1	3.8	ND	55.7		NM	
DY5-X-15	3753.87	Longmaxi Formation	Mudstone	0.81	NM	35.2	5.6	3.2	ND	56	0.388	1.534	1.922
DY5-X-16	3754.82	Longmaxi Formation	Mudstone		NM	34.3	5	2.9	1.6	56.2		NM	
DY5-X-17	3755.69	Longmaxi Formation	Silty mudstone		NM	36.1	5.2	4.2	ND	54.5	0.372	1.651	2.023
DY5-X-18	3756.72	Longmaxi Formation	Silty mudstone	0.87	NM	34.9	5.9	2.8	ND	56.4		NM	
DY5-X-19	3757.7	Longmaxi Formation	Silty mudstone	NM	3.9	33.3	4.8	2.7	ND	59.2	0.337	1.372	1.709
DY5-X-20	3758.9	Longmaxi Formation	Silty mudstone		NM	34.4	9.4	10.5	ND	45.7		NM	
DY5-X-21	3759.69	Longmaxi Formation	Silty mudstone	0.6	3	38.5	9.2	2.4	ND	49.9	0.392	1.274	1.666
DY5-X-22	3760.77	Longmaxi Formation	Silty mudstone		NM	38.6	8.5	7.2	ND	45.7		NM	
DY5-X-23	3761.8	Longmaxi Formation	Silty mudstone		NM	34	10.8	2.7	ND	52.5		NM	
DY5-X-24	3762.56	Longmaxi Formation	Silty mudstone	1.1	NM	34.7	8.4	2.6	ND	54.3	0.332	2.108	2.44
DY5-X-25	3763.83	Longmaxi Formation	Silty mudstone		NM	30.7	7.5	7.4	ND	54.4		NM	
DY5-X-26	3764.7	Longmaxi Formation	Silty mudstone		NM	32.7	8	7.2	ND	52.1	0.448	1.493	1.941
DY5-X-27	3765.82	Longmaxi Formation	Silty mudstone	1.26	NM	34.2	9.4	2.9	1.2	52.3		NM	
DY5-X-28	3766.7	Longmaxi Formation	Silty mudstone		NM	36.2	13.1	8.1	ND	42.6	0.446	2.059	2.505
DY5-X-29	3767.37	Longmaxi Formation	Silty mudstone		NM	34.8	8.9	3.2	1.3	51.8		NM	
DY5-X-30	3768	Longmaxi Formation	Silty mudstone	1.03	3.7	35.2	9.2	3.9	ND	51.7	0.381	0.539	0.92
DY5-X-31	3769.83	Longmaxi Formation	Silty mudstone		NM	23.1	5.6	30.4	ND	40.9	0.442	0.599	1.041
DY5-X-32	3770.29	Longmaxi Formation	Silty mudstone	NM	3.1	32.7	8.1	2.7	1.6	54.9		NM	
DY5-X-33	3771.71	Longmaxi Formation	Silty mudstone	1.03	NM	30.2	7.3	20.1	ND	42.4	0.402	0.618	1.02
DY5-X-34	3772.35	Longmaxi Formation	Silty mudstone		NM	35.6	10.9	6.1	ND	47.4		NM	
DY5-X-35	3773.74	Longmaxi Formation	Silty mudstone	1.13	2.2	38.4	10.1	0	ND	51.5	0.275	0.571	0.846
DY5-X-36	3774.37	Longmaxi Formation	Silty mudstone	1.42	3.9	35.5	8.4	7.2	1.6	47.3		NM	
DY5-X-37	3775.36	Longmaxi Formation	Silty mudstone		NM	37.6	9.9	3.7	1.7	47.1		NM	
DY5-X-38	3776.02	Longmaxi Formation	Silty mudstone	1.59	NM	33.8	9.1	4.8	2.2	50.1	0.448	1.382	1.83
DY5-X-39	3777.23	Longmaxi Formation	Silty mudstone		NM	32	9.3	12.5	ND	46.2		NM	
DY5-X-40	3778.26	Longmaxi Formation	Silty mudstone	1.26	3.3	38	10	5.3	ND	46.7	0.438	0.684	1.122
DY5-X-41	3779.35	Longmaxi Formation	Silty mudstone		NM	33.1	9.1	17.4	ND	40.4		NM	
DY5-X-42	3780.31	Longmaxi Formation	Silty mudstone	1.19	3.7	30.5	10	13.7	ND	45.8	0.294	0.816	1.11
DY5-X-43	3781.37	Longmaxi Formation	Silty mudstone		NM	32.3	10.3	15.2	ND	42.2		NM	

(*continued*)

Sample	Depth /m	Strata	Lithology	TOC /%	Porosity /%	Quartz /%	Feldspar /%	Carbonate /%	Pyrite /%	Clay /%	Desorbed gas /($m^3 \cdot t^{-1}$)	Lost gas /($m^3 \cdot t^{-1}$)	GIP /($m^3 \cdot t^{-1}$)
DY5-X-44	3782.46	Longmaxi Formation	Silty mudstone	1.31	3.8	36	10.9	9.8	2	41.3	0.431	0.885	1.316
DY5-X-45	3783.32	Longmaxi Formation	Silty mudstone	NM		27.5	8.9	13.5	1.3	48.8		NM	
DY5-X-46	3784.98	Longmaxi Formation	Silty mudstone	1.41	3.9	40.6	9.6	5.2	ND	44.6	0.472	1.454	1.926
DY5-X-47	3785.2	Longmaxi Formation	Silty mudstone	NM		35.3	10.6	7.5	1.7	44.9		NM	
DY5-X-48	3785.91	Longmaxi Formation	Silty mudstone	1.69	4.4	38.6	8.1	3.6	3	46.7	0.606	1.908	2.514
DY5-X-49	3787.2	Longmaxi Formation	Silty mudstone	2.04	NM	36.2	7.7	9	2.8	44.3	0.789	2.73	3.519
DY5-X-50	3788.33	Longmaxi Formation	Silty mudstone	NM	5.4	39.8	9.2	9	ND	42		NM	
DY5-X-51	3789.16	Longmaxi Formation	Silty mudstone	2.39	NM	36	7.1	3.8	2.5	50.6		NM	
DY5-X-52	3789.93	Longmaxi Formation	Carbonaceous shale	2.3	NM	41.5	8	8	3.1	39.4	0.806	2.959	3.765
DY5-X-53	3791.38	Longmaxi Formation	Carbonaceous shale	NM	4.3	34.7	6.6	25.5	ND	33.2		NM	
DY5-X-54	3791.97	Longmaxi Formation	Carbonaceous shale	2.34	NM	41.6	6.3	4.4	2.2	45.5	0.652	2.774	3.426
DY5-X-55	3793.8	Longmaxi Formation	Carbonaceous shale	2.23	4.6	43.1	6.5	3.6	5.1	41.7	0.811	3.636	4.447
DY5-X-56	3794.22	Longmaxi Formation	Carbonaceous shale	NM		40.8	7.5	4.6	2.3	44.8		NM	
DY5-X-57	3795.21	Longmaxi Formation	Carbonaceous shale	2.18	NM	41.4	6	4.8	3.5	44.3		NM	
DY5-X-58	3796.13	Longmaxi Formation	Carbonaceous shale	2.51	4.9	42.6	6.8	14.4	ND	36.2	0.835	4.351	5.186
DY5-X-59	3797.24	Longmaxi Formation	Carbonaceous shale	NM		42.9	4.9	7.5	2.7	42		NM	
DY5-X-60	3798.3	Longmaxi Formation	Carbonaceous shale	2.69	NM	43.7	5.3	7.5	2.3	41.2	0.675	4.422	5.097
DY5-X-61	3799.28	Longmaxi Formation	Carbonaceous shale	2.94	NM	44	5.3	8.4	3.1	39.2		NM	
DY5-X-62	3800.32	Longmaxi Formation	Carbonaceous shale	NM	5	46.6	4.7	9.2	ND	39.5	0.704	4.649	5.353
DY5-X-63	3801.2	Longmaxi Formation	Carbonaceous shale	2.84	5.4	39.3	3.9	9.5	2.3	45		NM	
DY5-X-64	3802.74	Longmaxi Formation	Carbonaceous shale	2.51	NM	38.5	ND	18.9	2.9	39.7	0.831	4.453	5.284
DY5-X-65	3803.2	Longmaxi Formation	Carbonaceous shale	NM		39.8	3.3	10.5	2.9	43.5		NM	
DY5-X-66	3804.34	Longmaxi Formation	Carbonaceous shale	2.03	4.8	44.9	5.3	5.1	2.5	42.2	0.958	5.342	6.3
DY5-X-67	3805.2	Longmaxi Formation	Carbonaceous shale	2.82	2.7	43	7.2	5.8	4.3	39.7		NM	
DY5-X-68	3806.28	Longmaxi Formation	Carbonaceous shale	NM		37.5	5.7	10.9	3	42.9		NM	
DY5-X-69	3807	Longmaxi Formation	Siliceous shale	3.31	NM	54.5	3.3	7.3	2.6	32.3	0.728	5.317	6.045
DY5-X-70	3808.8	Longmaxi Formation	Siliceous shale	4.32	6.3	50.8	5.4	3.7	5.3	34.8	1.071	7.247	8.318
DY5-X-71	3809.2	Longmaxi Formation	Siliceous shale	NM	6.5	50.4	5.2	8.1	3	33.3		NM	
DY5-X-72	3810.17	Longmaxi Formation	Siliceous shale	4.75	6.6	52.6	7.3	9.2	2.6	28.3		NM	
DY5-X-73	3811.47	Longmaxi Formation	Siliceous shale	4.99	7.3	57.7	7.6	9.9	3	21.8	1.231	8.851	10.082
DY5-X-74	3812.34	Longmaxi Formation	Siliceous shale	NM		63.2	8.9	2.1	1.8	24		NM	
DY5-X-75	3813.23	Wufeng Formation	Siliceous shale	4.42	5.7	71.3	ND	10.2	ND	18.5	1.269	11.469	12.738
DY5-X-76	3814.28	Wufeng Formation	Siliceous shale	4.71	5.8	53.8	ND	10.7	5.4	30.1		NM	
DY5-X-77	3815.33	Wufeng Formation	Siliceous shale	NM	5.5	58.9	2.6	7.3	ND	31.2	1.301	7.694	8.995
DY5-X-78	3816.26	Wufeng Formation	Siliceous shale	2.49	NM	61.6	2.8	0	ND	35.6		NM	
DY5-X-79	3817.3	Wufeng Formation	Siliceous shale	3.56	5.4			NM			1.164	6.255	7.419

Notes: NM, not measured; ND, not detected.

3.2.2 Total organic carbon

Total organic carbon (TOC) content was measured with the total carbon and sulfur Leco CS-230 analyzer, after removal of carbonate with dilute HCl, and analytical precision was better than 10%. This work was conducted at the State Key Laboratory of Shale Oil and Gas Enrichment Mechanisms and Effective Development.

3.2.3 X-ray diffraction

X-ray diffraction (XRD) measurements of powdered

whole-rock samples were conducted at the Analytical Laboratory of Beijing Research Institute of Uranium Geology using a Panalytical X'Pert PRO diffractometer equipped with a Cu-target tube and a curved graphite monochromator, operating at 40 kV and 40 mA. Samples were step-scanned from 3° to 70° with a step size of 0.02° (2θ). The relative mineral percentages were estimated semiquantitatively using the area under the curve for the major peaks of each mineral.

3.2.4 Porosity

Small cylindrical cores with a diameter of 25 mm and a length of 20 mm were drilled from the selected shale core samples. The cores were first dried at a temperature of 100°C for 24 h to remove any moisture and weighed, and then porosity was measured using the AP-608 Automated Permeameter-Porosimeter at the State Key Laboratory of Oil and Gas Reservoir Geology and Exploitation. Detailed analytical process was described by Lu et al. (2021).

3.2.5 Gas compositions

The shale gas was produced from the horizontal section of Well DY5 with burial depth of 4165–5685 m, and the gas compositions were measured at the Geological Center Laboratory of the Southwest Oil & Gas Field Company of Sinopec using an Agilent 7890B Gas Chromatograph (GC) System equipped with two thermal conductivity detectors (TCD) and one flame ionization detector (FID). Detailed analytical process was described by Li et al. (2021).

3.2.6 *In situ* gas desorption and calculation of the GIP content

The *in situ* gas desorption of fresh core samples was conducted using a rapid field desorption apparatus (WXC-2) designed by the Wuxi Research Institute of Petroleum Geology, Sinopec Petroleum Exploration & Production Research Institute, and the detailed principle and analytical processes were described by previous authors (Lu et al., 2021). The desorption processes include natural desorption and heating desorption. The former was conducted under the condition of mud circulation temperature (56°C), and the latter was carried out at the higher temperature up to 110°C. The gas obtained from these desorption processes is categorized as the desorbed gas. The lost gas content was calculated by the polynomial regression fitting method of the first 3 h data from natural desorption (e.g., Sun et al., 2020). The GIP content is the sum of the desorbed gas and lost gas.

4 Results

4.1 Bulk organic geochemistry

TOC value of the studied WF−LMX shale samples ranges from 0.57% to 4.99%, averaging 2.15% (n = 40; Table 1; Fig. 2). In general, the TOC value displays a decreasing tendency up-section. The shale samples recovered from the WF and the lower part of the LMX display higher TOC values, generally > 2%, while the upper part of the LMX exhibits a relatively low value (generally < 2%; Fig. 2).

4.2 Mineralogical compositions

The studied WF–LMX shale is dominated by quartz and clay, with a small quantity of feldspar, carbonate, and pyrite (Table 1; Fig. 2). Among them, the feldspar is predominantly composed of plagioclase; the carbonate primarily consists of dolomite, secondly by calcite (Table 1). The quartz content displays a similar trend with the TOC value, which has higher values (up to 71.3%) in the WF shale and the lower part of LMX shale, and gradually decreases to 27% up-section of LMX shale (Fig. 2). In contrast, the clay content shows a reverse tendency, and the upper part of the LMX has higher clay contents up to 59.2% (Fig. 2).

4.3 Porosity and pore types

The measured porosity of the studied WF–LMX shale samples ranges from 2.2% to 7.3%, averaging 4.5% (n = 32; Table 1; Fig. 2), which also displays a similar trend with the TOC value (Fig. 2). The higher porosities (> 4%) are displayed in the WF and the lower part of the LMX Formation, while the relatively low porosities (< 4%) are showed in the upper part of the LMX Formation (Fig. 2).

SEM observations revealed that the pores in the studied WF–LMX shale samples was dominated by organic matter (OM) pores (Figs. 3(a)–3(c)). In especial, abundant microcrystalline quartz (so-called "microquartz") and nano-sized quartz grains have been found in the organic-rich siliceous shales, and a large volume of OM pores has been observed in the depositional OM and migrated OM (i.e., solid bitumen) between these quartz grains (Figs. 3(a) and 3(b)). The porous solid bitumen was also occurred in the interparticle pores of other detrital minerals (e.g., feldspar) and the intraparticle pores of pyrite framboids and clay platelets (Figs. 3(c)–3(e)). Inorganic pores mainly include clay mineral pores, mineral intraparticle pores, and micro-fractures (Figs. 3(d)–3(f)). Clay mineral pores were widely developed in the clay-rich shale samples (Figs. 3(d) and 3(f)). Although some of these pores were filled with migrated OM, a substantial amount of them was empty (Fig. 3(e)). Mineral intraparticle pores mainly include dissolution pores of carbonates (e.g.,

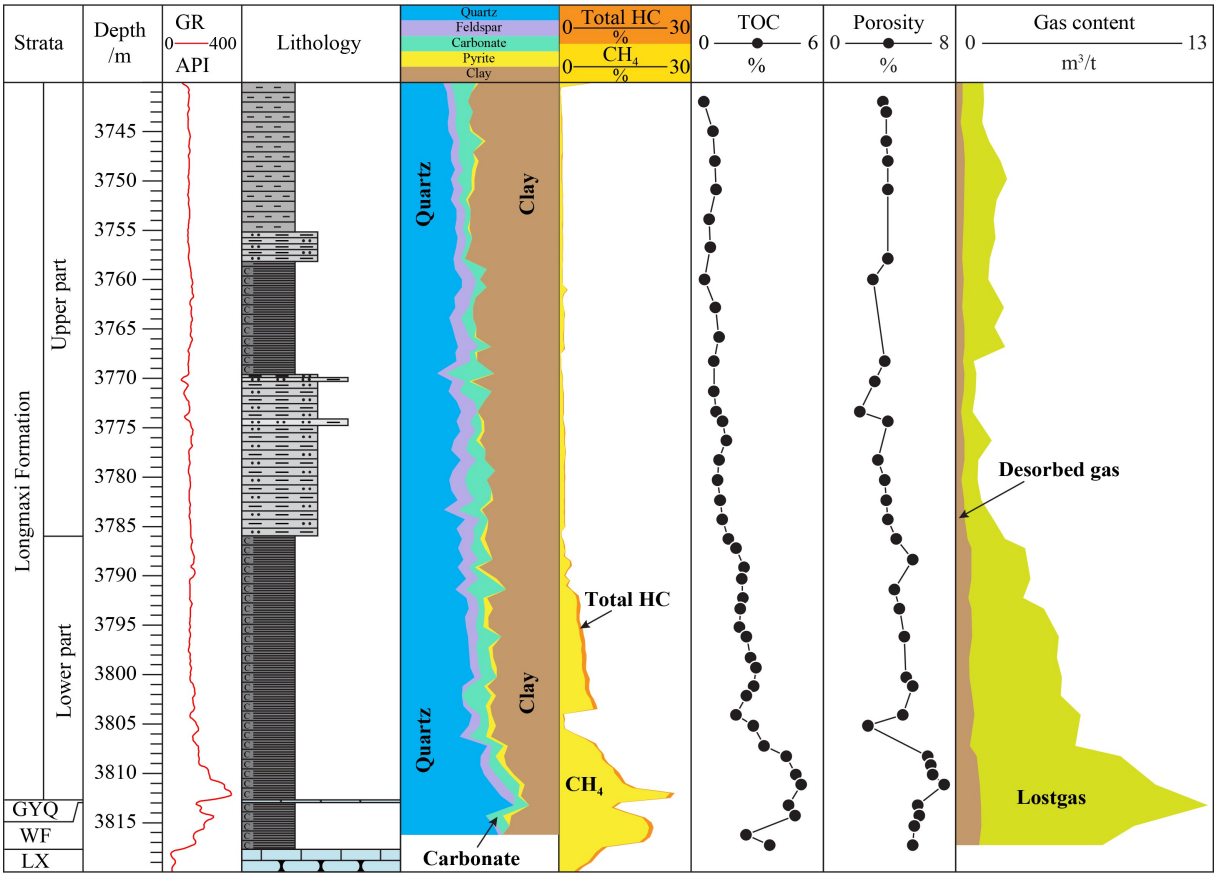

Fig. 2 Vertical profiles showing mineral compositions, gas logging, TOC content, porosity, and gas contents of the Wufeng–Longmaxi Formations from the Well DY5. Total HC = Total hydrocarbon. See detailed lithology legend in Fig. 1.

ferrodolomite) (Fig. 3(f)). In addition, micro-fractures were usually observed along the bedding planes or between mineral grains (Fig. 3(e)), which may be related to the shrinking of clay minerals and/or decompression effect of the shale samples after the core uplifting (Chalmers et al., 2012).

4.4 GIP content and gas compositions

The contents of lost gas, desorbed gas and GIP of the studied shale samples are listed in Table 1. The GIP content varies from 0.85 to 12.7 m^3/t (average = 3.5 m^3/t, n = 39; Fig. 2). The desorbed gas content ranges from 0.25 to 1.30 m^3/t (average = 0.6 m^3/t, n = 39; Fig. 2). The lost gas content dominates the GIP content, ranging from 0.54 to 11.5 m^3/t (average = 2.9 m^3/t, n = 39; Fig. 2). The greater content of lost gas may be resulted from greater burial depths and long times for the acquisition of core samples. Overall, the GIP content displays higher values in the WF Formation and the lower part of the LMX Formation, and gradually decreases up-section (Fig. 2). The gas logging also shows a similar tendency (Fig. 2).

The WF–LMX shale gas compositions of the Well DY5 are listed in Table 2. The hydrocarbon gas is composed of methane, ethane, and propane, while the methane is dominant (average = 98.3%; n = 9). The ethane and propane contents are very low, with an average of 0.56% and 0.02%, respectively. The non-hydrocarbon gas mainly consists of CO_2 and N_2, with average of 0.70% and 0.40%, respectively. A smaller proportion of He and H_2 (< 0.03%) is also detected. Overall, the shale gas can be classified as dry gas (CH_4 > 95%), with small amounts of non-hydrocarbon gases (e.g., CO_2 and N_2).

5 Discussion

5.1 Control of TOC on porosity and GIP

Previous studies suggested that the GIP content of shale was controlled by the porosity (e.g., Ross and Bustin, 2002), and some authors found that the porosity was mainly influenced by TOC contents (Milliken et al., 2013; Tian et al., 2013; Sun et al., 2020). In our study, the porosity of the WF–LMX shale displays a strong positive correlation with the TOC content (r = + 0.96, $p(\alpha)$ < 0.01), excluding two outliers of low porosity (Fig. 4). Such a positive relationship suggests that the porosity of the studied shale is predominately composed of organic porosity, and significantly increases with the increasing TOC content, with an average increase of 0.75% porosity

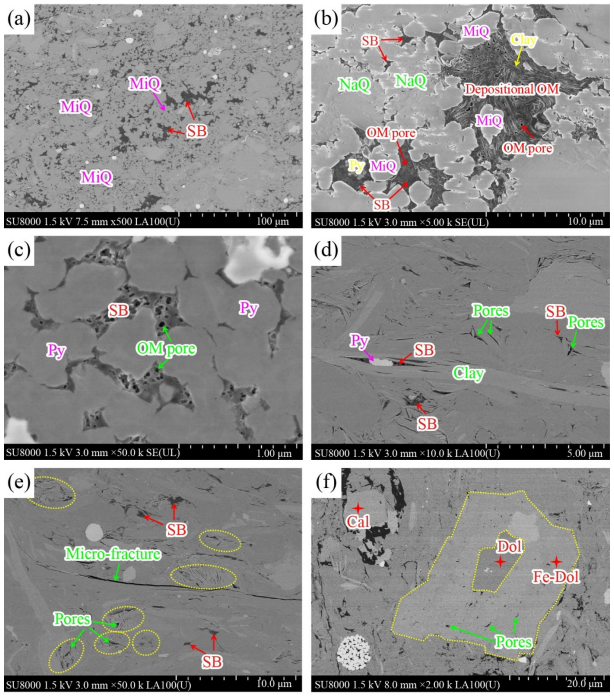

Fig. 3 SEM photographs illustrating various pore types in the studied WF-LMX shales from the Well DY5. Points delineated by red stars were analyzed by EDS. Notes: OM = organic matter; SB = solid bitumen; MiQ = microquartz; NaQ = nano-quartz; Py = pyrite; Cal = calcite; Dol = dolomite; Fe-Dol = ferrodolomite. (a) Siliceous shale is mainly composed of abundant microquartz grains, and a large volume of matrix-dispersed OM (probably migrated solid bitumen) was widely developed in the interparticle pores of authigenic microquartz grains. WF, 3813.6 m. (b) Interparticle pores of microquartz and nano-quartz particles are filled with the migrated OM (i.e., solid bitumen), and the linear clay minerals are usually occurred in the depositional OM (possibly alginite). Abundant OM pores can be observed in the migrated and depositional OM. WF, 3813.6 m. (c) Intraparticle pores of a pyrite framboid were filled with the SB, and abundant pores are developed within the SB. LMX, 3809.7 m. (d) Abundant intraparticle pores were developed within clay platelets, some of which were filled with porous solid bitumen and diagenetic pyrite grains. LMX, 3759.4 m. (e) Interparticle pores of detrital grains were filled with porous solid bitumen, while a large amount of intraparticle pores were developed within clay platelets (indicated by yellow dashed circles). A micro-fracture was developed along the bedding plane. LMX, 3759.4 m. (f) Few carbonate grains, including calcite and dolomite, were occurred in the shale. A dolomite grain was composed with the dolomite core and the ferrodolomite rim, and irregular intraparticle pores (or dissolved pores) were developed within the ferrodolomite rim. LMX, 3791.4 m.

per an increase of 1% TOC. The porosity of the WF–LMX shale exhibits strong positive correlations with the GIP and desorbed gas contents, respectively (Fig. 5(a)). Moreover, the TOC content of shale also displays strong positive relationships with the GIP and desorbed gas contents, respectively (Fig. 5(b)). It can be inferred that the TOC content of shale can directly affect the GIP content by increasing organic porosity for methane storage. SEM observations have also found that abundant pores with variable diameters are developed within the

Table 2 Gas compositions of the WF–LMX shale gas from the horizontal section of Well DY5

Sample	Depth/m	Gas composition/%						
		Methane	Ethane	Propane	N_2	He	H_2	CO_2
1	4165.00–5685.00	98.31	0.56	0.02	0.39	0.02	0.00	0.69
2	4165.00–5685.00	98.34	0.55	0.02	0.39	0.02	0.00	0.67
3	4165.00–5685.00	98.29	0.57	0.02	0.42	0.03	0.00	0.65
4	4165.00–5685.00	98.33	0.55	0.02	0.39	0.02	0.00	0.68
5	4165.00–5685.00	98.31	0.53	0.02	0.44	0.03	0.00	0.65
6	4165.00–5685.00	98.25	0.59	0.02	0.36	0.02	0.00	0.75
7	4165.00–5685.00	98.18	0.59	0.02	0.42	0.02	0.00	0.76
8	4165.00–5685.00	98.23	0.59	0.02	0.36	0.02	0.00	0.76
9	4165.00–5685.00	98.32	0.54	0.02	0.39	0.03	0.01	0.70
Average		98.28	0.56	0.02	0.40	0.023	0.0011	0.70

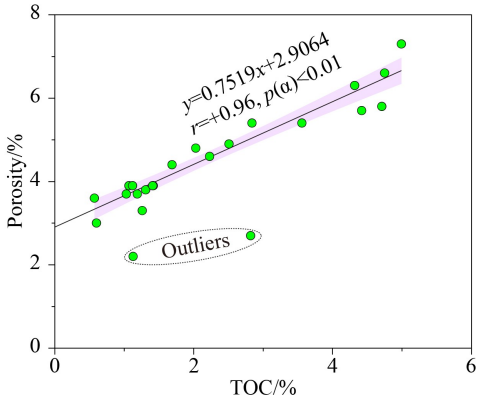

Fig. 4 Cross-plot of TOC content and porosity of the studied WF–LMX shales from the Well DY5. Regression lines (solid) with 95% confidence intervals (pink zones) are shown. r = Pearson correlation coefficient; $p(\alpha)$ = significance.

migrated solid bitumen and depositional OM (Figs. 3(b)–3(d)). These nano-sized OM pores could provide a large amount of absorption sites for methane (Ambrose et al., 2012; He et al., 2019a). Previous works have reported that the studied WF–LMX shale reservoirs of the Well DY5 are still under an overpressure system, with formation pressure coefficient of 1.82 (Guo et al., 2020), so the shale gas may be composed of free gas and adsorbed gas. According to the geological model of the GIP of an LMX shale sample (TOC = 3.98%) from the Well PY1 (Pan et al., 2016), the adsorbed gas accounts for approximately 50% of the GIP at a pressure coefficient of 1.5 and a burial depth of 4000 m. During the uplifting of core samples, free gas of shale may be largely lost, and the desorbed gas may be mainly composed of adsorbed gas, thus leading to lower contents of desorbed gas.

It has been widely accepted that the TOC content is a critical parameter for estimating the enrichment degree of shale gas fields because it is always positively correlated with the GIP contents (Jarvie, 2004; Guo, 2014; Zhao

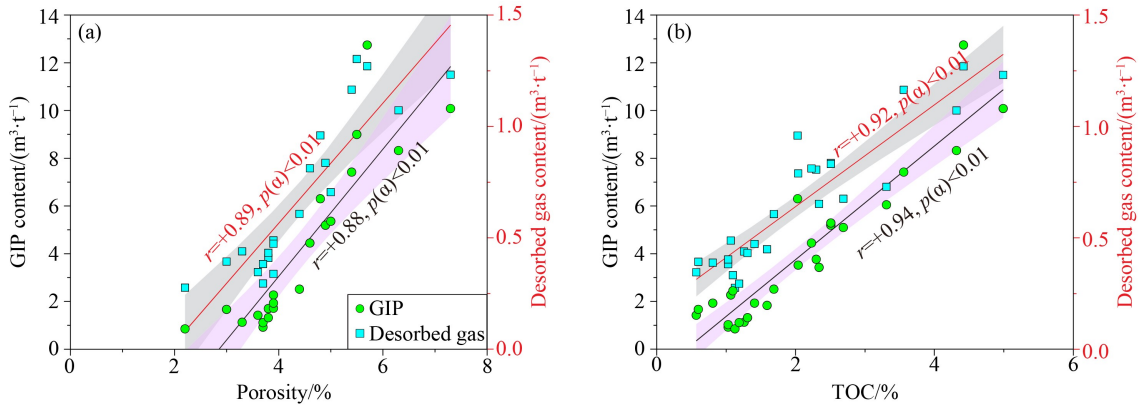

Fig. 5 Cross-plots of the GIP/desorbed gas contents versus (a) the TOC content and (b) the porosity value of the studied WF–LMX shales from the Well DY5. Regression lines (solid) with 95% confidence intervals (pink and grey zones) are shown.

et al., 2017b; Qiu and Zou, 2020; Sun et al., 2020, 2021b). Moreover, the TOC content greater than 2% has been used for a lower limit of commercial shale gas reservoirs (e.g., Wang et al., 2012; Qiu and Zou, 2020). In the Fuling Shale Gas Field, the GIP content of the WF–LMX shale samples with the TOC content greater than 2% is generally larger than 3.5 m^3/t (Guo, 2014), which exceeds the lower limit of commercial shale gas reservoirs (i.e., 2 m^3/t; Wang et al., 2012). However, such a lower limit of the GIP content of commercial deep shale gas reservoirs may be increased due to higher costs. As a commercially-exploited deep shale gas field, the Haynesville shale has an average GIP content of 5.38 m^3/t (Jarvie, 2012). In our study, the WF–LMX deep shale from the Well DY5 is estimated to have the GIP content greater than 5 m^3/t when the TOC content is larger than 2.5% (Fig. 5(b)). Although a TOC threshold for commercial exploitation of deep shale gas is very hard to be proposed in this study, the TOC content greater than 2.5% may be a conservative option for deep shale gas exploration and development.

5.2 Influence of mineral compositions on GIP

Inorganic mineral compositions have suggested to be critical to reservoir properties of shale, including porosity and rock mechanical properties, thus exerting a significant effect on shale gas production (e.g., Jarvie, 2004; Jarvie et al., 2007; Milliken et al., 2013; Zhao et al., 2017a; Dong et al., 2019). The cross-plots between gas contents and the contents of major mineral compositions (e.g., quartz, clay, feldspar, and carbonate) of the studied WF–LMX shale samples are presented in Fig. 6. The GIP content and desorbed gas content display excellent positive correlations with the quartz content (Fig. 6(a)), but exhibit good negative correlations with the clay content (Fig. 6(b)). The feldspar and carbonate contents have no obvious correlations with gas contents (Figs. 6(c) and 6(d)), suggesting that the influences of them on the gas content of studied shale are less. It appears that the quartz content has directly controlled the gas content of shale. However, a good positive relationship between quartz and TOC contents has been observed in our studied samples (Fig. 7(a)) and previous studies (Guo, 2014; Dong et al., 2019; Khan et al., 2019; Xi et al., 2019), which has usually been attributed to the flourishing of siliceous organisms (mostly radiolarians) (Khan et al., 2019). Similarly, a good negative relationship between clay and TOC contents has been presented in our study (Fig. 7(c)), suggesting that the clay played a dilution role in organic matter accumulation. Therefore, the TOC content still directly controls the gas content of the WF–LMX deep shale, which is consistent with the shallow gas shale reservoirs (e.g., Guo, 2014; Zhao et al., 2017b; Sun et al., 2020).

Previous studies have revealed that the inorganic pores within quartz, feldspar, and carbonate minerals have low adsorption capacities of methane (Ross and Marc Bustin, 2009), but clay minerals have showed to have large adsorption capacities of methane due to widespread of nano-pores (Ross and Marc Bustin, 2009; Ji et al., 2012; Hou et al., 2014). Ji et al. (2012) have found that the maximum methane adsorption capacities of illite/smectite mixed layer, chlorite and illite can be up to 3.66 m^3/t, 2.07 m^3/t and 1.59 m^3/t, respectively. Hou et al. (2014) also have found that the LMX shale samples with low TOC values (as low as 0.16%) recovered from the Well HY1 displayed the relatively high adsorption capacities of methane (up to 2.11 m^3/t). To explore the influence of clay on the porosity and GIP of studied shale samples, the TOC-normalized parameters (porosity/TOC and GIP/TOC ratios) have been introduced. The porosity/TOC ratio shows a good exponential function with the clay content, indicating that clay minerals have some contributions to the inorganic porosity of shale samples, especially clay-rich shale samples (Fig. 8(a)). The GIP/TOC ratio displays an overall decreasing trend with the increasing clay contents (Fig. 6(b)), suggesting that the clay plays a negative role in the gas content contributed from inorganic porosity. As mentioned above, the clay may have contributed to the gas content of clay-rich shale samples due to the presence of abundant adsorption sites for methane (e.g., Ji et al., 2012; Hou et al., 2014). Some authors have suggested that connate water was mainly occurred in the intraparticle pores of clay minerals (Yang

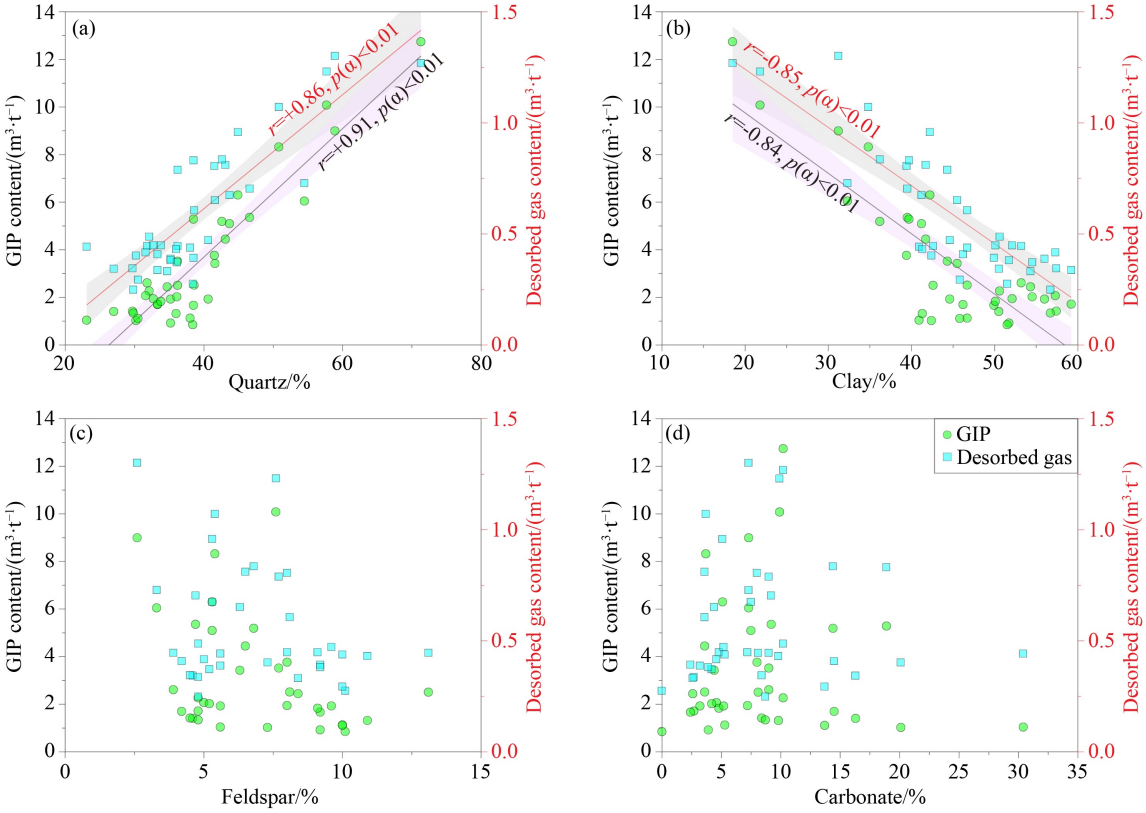

Fig. 6 Cross-plots of the GIP/desorbed gas contents versus (a) quartz content, (b) clay content, (c) feldspar content, and (d) carbonate content of the studied WF–LMX shales from the Well DY5. Regression lines (solid) with 95% confidence intervals (pink and grey zones) are shown.

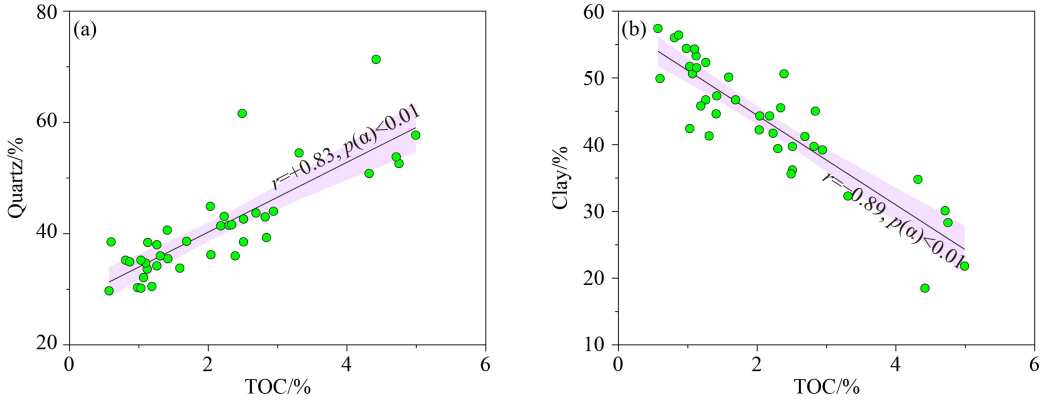

Fig. 7 Cross-plots of the TOC content versus (a) quartz content, and (b) clay content of the studied WF–LMX shales from the Well DY5. Regression lines (solid) with 95% confidence intervals (pink zones) are shown.

et al., 2020; Gao et al., 2022), which would greatly decrease the GIP content of shale (e.g., Cheng et al., 2017; Sun et al., 2020, 2021a, 2021b). Although a large volume of inorganic pores was observed within the clay platelets of clay-rich shale samples (Fig. 3(e)), the presence of connate water would decrease the adsorption capacities of methane thus resulting in the lower GIP/TOC ratios in clay-rich shales. Nevertheless, several outliers of clay-rich shale samples show the relatively high GIP/TOC ratios (Fig. 7(b)), suggesting that clay might still have a certain contribution to the GIP content of deep shale, especially clay-rich shale samples.

5.3 Implication for deep and ultra-deep shale gas exploration

Previous studies have reported that the commercially-exploited deep shale gas fields in the United States (e.g.,

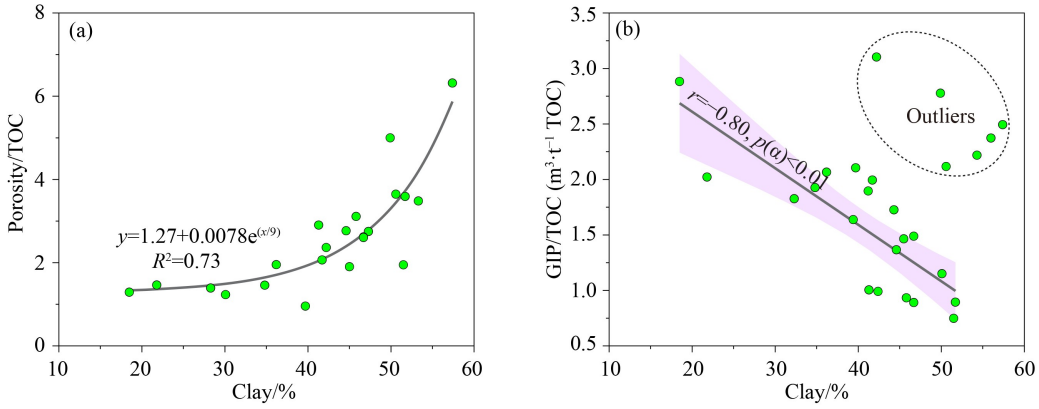

Fig. 8 Cross-plots of the clay content versus (a) porosity/TOC ratio, and (b) GIP/TOC ratio of the studied WF–LMX shales from the Well DY5. Regression lines (solid) with 95% confidence intervals (pink zone) are shown.

Haynesville, Eagle Ford and Cana Woodford) are generally characterized by high porosity, high GIP content, moderate maturity, and high brittleness (Jarvie, 2012; Abou-Sayed et al., 2011). The porosity of shale reservoirs is still a critical parameter for evaluating the GIP content (Fig. 5(a)). Although inorganic porosity generally shows a decreasing trend with the increasing burial depths (Xiao et al., 2015; Hall, 2019), organic porosity may increase due to the increasing maturity of OM (Mastalerz et al., 2013; Xiao et al., 2015). Previous authors have reported that the bitumen reflectance (BR_o) of the LMX shale samples recovered from the Well DY2, close to our studied well, is averaged at approximately 2.88% (Yang, 2016). The equivalent vitrinite reflectance ($EqVR_o$) calculated from the BR_o values using the equation of Schoenherr et al. (2007) was approximately 2.98%, suggesting that the LMX shale in the Dingshan area is currently in the thermally overmature stage. Xiao et al. (2015) proposed a model for porosity evolution of the Lower Paleozoic shale in south China and suggested that the increase of organic porosity may be diminished at the $EqVR_o$ value of about 3.5%. Thus, organic porosity of studied WF–LMX shale samples was largely preserved and was not involved into the destruction stage.

The measured porosity of the WF–LMX deep shale reservoirs in Dingshan area is still relatively high, ranging from 2.2 to 7.3% (average = 4.5%, n = 32; Table 1), close to 2.2%–8.0% reported in the Yongchuan deep shale gas field (i.e., Well YY1; He et al., 2020), although it is lower than that of the Haynesville Shale Gas Field (4.0%–14.0%, average = 8.3%; Jarvie, 2012). However, deep shale reservoirs display higher porosity relative to mid-shallow gas shale reservoirs (e.g., Jiaoshiba shale and Barnett shale; Fig. 9; Jarvie, 2012; Zhao et al., 2017b; He et al., 2020). The WF–LMX ultra-deep shale reservoirs still display higher porosity, e.g., 0.6%–6.7% of the Well PS1 (Fig. 9; data provided by the Sinopec Exploration Branch Company). Some authors suggested that the dissolution pore might be accounted for the high porosity of deep shale reservoirs (e.g., Nie et al., 2019b; He et al., 2020). However, organic pore appears to be a predominant pore type in the studied organic-rich shale samples (Figs. 3(b)–3(d)), which is also supported by an excellent positive correlation of TOC content and porosity (Fig. 4). Additionally, numerous studies have showed that authigenic quartz plays a critical role in the protection of organic porosity during the burial (e.g., Zhao et al., 2017a; Dong et al., 2019; Xi et al., 2019; Longman et al., 2019). In our study, the aggregates of amorphous to euhedral microquartz formed a rigid framework in organic-rich siliceous shales and could provide a shield for the development and preservation of OM pores within the depositional and migrated OM under the deeper burial and strong compaction (Figs. 3(a) and 3(b)). Therefore, organic porosity of deep gas shale reservoirs appears to be largely preserved due to

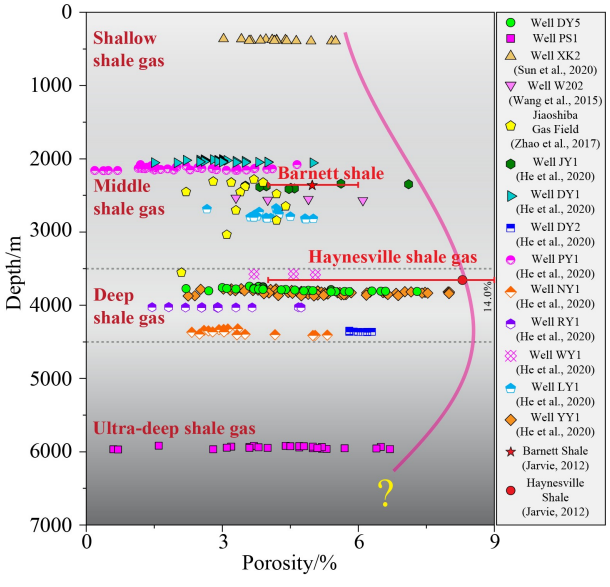

Fig. 9 Vertical variation of the porosity value of the WF–LMX shale from the Sichuan Basin with the increasing burial depths (Guo, 2014; Wang et al., 2015; Zhao et al., 2017; He et al., 2020; Sun et al., 2020). Data of the Well PS1 are provided from the Sinopec Exploration Branch Company. Data of the Barnett shale and the Haynesville shale are from Jarvie (2012).

widespread occurrence of authigenic quartz, thus resulting in higher total porosity.

The GIP content of the WF–LMX shale in the Sichuan Basin shows a similar trend with the porosity (Fig. 10). The GIP content of shallow shale reservoirs is relatively low, generally < 3 m^3/t (e.g., Sun et al., 2020; Li et al., 2021). However, the GIP content displays a sharp increasing trend from shallow to middle shale reservoirs (Fig. 10). For example, the GIP content of the WF–LMX shale from the Jiaoshiba Shale Gas Field varies from 1.45 to 8.83 m^3/t (average = 4.25 m^3/t, n = 31; Guo, 2014). The Barnett shale reservoirs at similar burial depths (about 2348 m) also have similar GIP contents, ranging from 1.98 to 7.05 m^3/t (average = 5.39 m^3/t, n = 10; Jarvie, 2004). The GIP content of deep shale reservoirs is gradually increasing. Especially, the high-quality shale intervals recovered from the WF and lower part of the LMX of Well DY5 display larger GIP contents, as high as 12.7 m^3/t (Fig. 10), which are even greater than the GIP contents of 2.83–8.50 m^3/t for the commercially-exploited deep gas shale reservoir, i.e., the Haynesville shale (average burial depth of 3658 m) (Jarvie, 2012; Farinas and Fonseca, 2013; Chen and Zeng, 2016). With the increasing burial depth, the GIP content of ultra-deep shale reservoirs slightly increases (Fig. 10), which varies from 0.92 to 13.7 m^3/t, with average of 7.4 m^3/t (n = 23; data provided by the Sinopec Exploration Branch Company). Such high GIP contents suggest that a large volume of gas has been preserved in the deep and ultra-deep shale reservoirs, revealing great potentials of deep and ultra-deep shale gas.

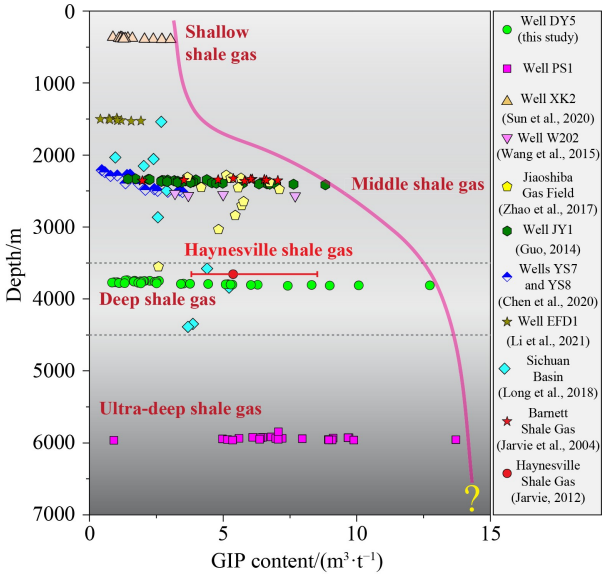

Fig. 10 Vertical variation of the GIP content of the WF−LMX shale from the Sichuan Basin with the increasing burial depths (Guo, 2014; Wang et al., 2015; Zhao et al., 2017; Long et al., 2018; Chen et al., 2020; Sun et al., 2020; Li et al., 2021). Data of the Well PS1 are provided from the Sinopec Exploration Branch Company. Data of the Barnett shale and the Haynesville shale are from Jarvie et al. (2004) and Jarvie (2012), respectively.

It's widely accepted that the porosity and GIP content of gas shale reservoirs are directly controlled by the TOC content (Jarvie, 2004; Guo, 2014; Sun et al., 2020, 2021b). Moreover, the GIP content of the WF–LMX shale in the Sichuan Basin is generally positively correlated with the porosity (Fig. 11), which should be mainly linked to widespread OM pores in shale (Figs. 3(b)–3(d)). Interestingly, a cross-plot of the GIP content versus the TOC content of the WF–LMX shale from the Sichuan Basin and the Barnett shale revealed a good linear relationship between the GIP and TOC contents in majority of shale samples, but the slope (k) values are varied (Fig. 12). The k value of shallow gas shale reservoirs is generally less than 0.5 (e.g., Sun et al., 2020; Li et al., 2021). With the increasing burial depths, the k value increases to 0.5–2.0 for the shale reservoirs at middle depths. For example, the k value of the WF–LMX

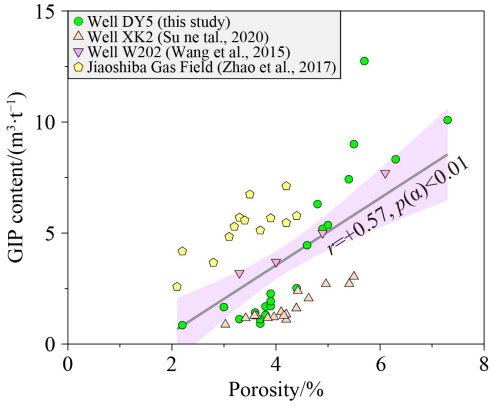

Fig. 11 Cross-plot of GIP content and porosity of the WF–LMX shales at varied burial depths from the Sichuan Basin (Wang et al., 2015; Zhao et al., 2017; Sun et al., 2020). Regression lines (solid) with 95% confidence interval (pink zone) are shown.

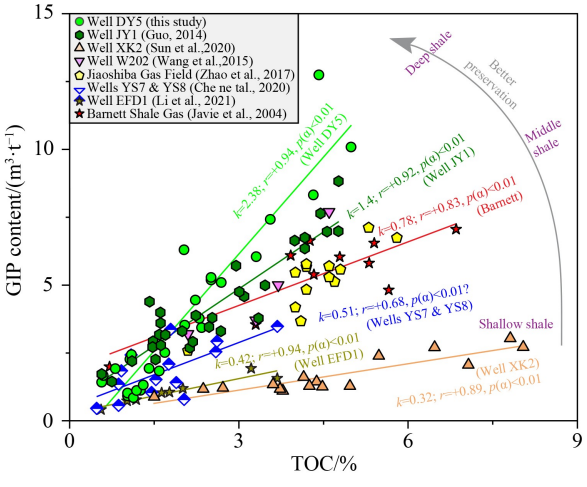

Fig. 12 Cross-plot of GIP and TOC contents of the WF–LMX shale reservoirs at varied burial depths from the Sichuan Basin (Guo, 2014; Wang et al., 2015; Zhao et al., 2017; Chen et al., 2020; Sun et al., 2020; Li et al., 2021) and the Barnett shale reservoir from the United State (Jarvie et al., 2004).

shale samples from the Well JY1 in the Jiaoshaoba Shale Gas Field is 1.4, representing that the GIP content increases by approximately 1.4 m^3/t per an increase of 1% TOC, which is also higher than that of the Barnett Shale (Jarvie, 2004). The *k* value of deep gas shale reservoirs is greater than 2.0, which is higher than that of mid-shallow gas shale reservoirs, implying better preservation of gas in shale with the increasing depths (Fig. 12). The *k* value of ultra-deep shale reservoirs may also increase, but more data are required to support it. Nevertheless, triaxial rock mechanical experiments revealed that the WF–LMX shale with burial depth of 3500–5000 m was still at the state of brittle-ductile transition (He et al., 2019b). However, the shale with burial depth greater than 5000 m would be at the ductile state (He et al., 2019b) and hydraulic fracturing of ultra-deep shale would be challenged under high temperature and high pressure, and more costs would also be required for shale gas exploration and development. Therefore, further work should be done on the controlling factors of the GIP content and gas exploitability evaluation for the ultra-deep shale in the Sichuan Basin.

6 Conclusions

1) The WF–LMX deep shale recovered from Dingshan area of the Sichuan Basin have relatively high GIP contents, ranging from 0.85 to 12.7 m^3/t. Shale gas is enriched with methane (CH_4 > 95%), with small amounts of non-hydrocarbon gases (e.g., CO_2 and N_2).

2) The OM pore is widespread and the dominant pore type in the WF–LMX deep organic-rich siliceous shale, and authigenic quartz plays a critical role in the protection of organic pores from compaction. Clay-hosted pore is the dominant pore type in clay-rich shale. The TOC content directly controls the GIP content of the deep shale via the increase of organic porosity, and clay minerals generally play a negative role in the GIP content.

3) The WF–LMX deep and ultra-deep shales in Sichuan Basin display greater porosity values and GIP contents due to the widespread of organic pores and better preservation, revealing great potentials of shale gas. From the perspective of rock mechanical properties, deep shale is the favorable exploration target at present, and the exploration and development of ultra-deep shale gas are still challenging.

Acknowledgments We are grateful to three anonymous reviewers for their comments that greatly improved the manuscript. This work was supported by the National Natural Science Foundation of China (Grant Nos. U19B6003-03-01 and 42030804) and the Fundamental Research Funds for the Central Universities (No. 2652019101).

References

Abou-Sayed I S, Sorrell M A, Foster R A, Atwood E L, Youngblood D R (2011). Haynesville Shale development program—from vertical to horizontal. In: North American Unconventional Gas Conference and Exhibition. Woodlands, June 14–16

Ambrose R J, Hartman R C, Diaz-Campos M, Akkutlu I Y, Sondergeld C H (2012). Shale gas-in-place calculations part I: new pore-scale considerations. SPE J, 17(01): 219–229

Bustin R M, Bustin A, Ross D (2009). Shale gas opportunities and challenges. In: Search and Discovery Articles 40382

Chalmers G R L, Bustin R M (2007). The organic matter distribution and methane capacity of the Lower Cretaceous strata of Northeastern British Columbia. Int J Coal Geol, 70(1−3): 223–239

Chalmers G R L, Bustin R M, Power I M (2012). Characterization of gas shale pore systems by porosimetry, pycnometry, surface area, and field emission scanning electron/transmission electron microscopy image analyses: examples from the Barnett, Woodford, Haynesville, Marcellus, and Doig unit. AAPG Bull, 96(6): 1099–1119

Chen S, Wang H, Wang Y, Jiang T, Zhang Y, Gong Z (2021). Differences in shale gas accumulation process and its significance in exploration of Lower Silurian Longmaxi Formation in northeast Yunnan. Front Earth Sci, 15(2): 343–359

Chen X, Rong J, Li Y, Boucot A J (2004). Facies patterns and geography of the Yangtze region, south China, through the Ordovician and Silurian transition. Palaeogeogr Palaeoclimatol Palaeoecol, 204(3−4): 353–372

Chen Z, Zeng Y (2016). Present situations and prospects of multi-stage fracturing technology for deep shale gas development. Pet Drill Tech, 44: 6−11 (in Chinese)

Chen Z, Chen L, Wang G, Zou C, Jiang S, Si Z, Gao W (2020). Applying isotopic geochemical proxy for gas content prediction of Longmaxi shale in the Sichuan Basin, China. Mar Pet Geol, 116: 104329

Cheng P, Tian H, Xiao X, Gai H, Li T, Wang X (2017). Water distribution in overmature organic-rich shales: implications from water adsorption experiments. Energy Fuels, 31(12): 13120–13132

Dong D, Gao S, Huang J, Guan Q, Wang S, Wang Y (2014). A discussion on the shale gas exploration and development prospect in the Sichuan Basin. Nat Gas Ind, 34(12): 1−15 (in Chinese)

Dong T, He S, Chen M, Hou Y, Guo X, Wei C, Han Y, Yang R (2019). Quartz types and origins in the paleozoic Wufeng–Longmaxi Formations, eastern Sichuan Basin, China: implications for porosity preservation in shale reservoirs. Mar Pet Geol, 106: 62–73

Farinas M, Fonseca E (2013). Hydraulic fracturing simulation case study and post frac analysis in the Haynesville Shale. In: SPE Hydraulic Fracturing Technology Conference. Woodlands, Texas: USA

Gao P, Xiao X, Hu D, Liu R, Cai Y, Yuan T, Meng G (2022). Water distribution in the ultra-deep shale of the Wufeng−Longmaxi Formations from the Sichuan Basin. Energies 15: 2215

Guo T (2021). Progress and research direction of deep shale gas exploration and development. Reservoir Eval. Dev, 11: 1−6 (in Chinese)

Guo T L, Zhang H R (2014). Formation and enrichment mode of Jiaoshiba shale gas field, Sichuan Basin. Pet Explor Dev, 41(1): 31–40

Guo X (2014). Rules of two-factor enrichment for marine shale gas in southern China—understanding from the Longmaxi Formation shale gas in Sichuan Basin and its surrounding area. Acta Geol Sin, 88: 1209−1218 (in Chinese)

Guo X, Hu D, Huang R, Wei Z, Duan J, Wei X, Fan X, Miao Z (2020). Deep and ultra-deep natural gas exploration in the Sichuan Basin: progress and prospect. Natur Gas Ind, 7(5): 419−423 (in Chinese)

Hall C D (2019). Compositional and diagenetic controls on brittleness in organic siliceous mudrocks. In: Camp W K, Milliken K L, Taylor K, Fishman N, Hackley P C, Macquaker J H S eds., Mudstone Diagenesis: Research Perspectives for Shale Hydrocarbon Reservoirs, Seals, and Source Rocks. AAPG Memoir 120

Hao F, Zou H, Lu Y (2013). Mechanisms of shale gas storage: implications for shale gas exploration in China. AAPG Bull, 97(8): 1325–1346

He Q, Dong T, He S, Zhai G (2019a). Methane adsorption capacity of marine-continental transitional facies shales: the case study of the Upper Permian Longtan Formation, northern Guizhou Province, southwest China. J Petrol Sci Eng, 183: 106406

He Z, Li S, Nie H, Yuan Y, Wang H (2019b). The shale gas "sweet window": "the cracked and unbroken" state of shale and its depth range. Mar Pet Geol, 101: 334–342

He Z, Nie H, Hu D, Jiang T, Wang R, Zhang Y, Zhang G, Lu Z (2020). Geological problems in the effective development of deep shale gas: a case study of Upper Ordovician Wufeng−Lower Silurian Longmaxi Formations in Sichuan Basin and its periphery. Acta Petrol Sin, 41: 379−391 (in Chinese)

Hou Y, He S, Yi J, Zhang B, Chen X, Wang Y, Zhang J, Cheng C (2014). Effect of pore structure on methane sorption potential of shales. Pet Explor Dev, 41(2): 272–281

Jarvie D M (2004). Evaluation of hydrocarbon generation and storage in Barnett shale, Fort Worth Basin, Texas. Texas: Humble Geochemical Services Division

Jarvie D M (2012). Shale resource systems for oil and gas: part I—shale-gas resource systems. In: Breyer J A ed., Shale Reservoirs—Giant Resources for the 21st Century: AAPG Memoir 97

Jarvie D M, Hill R J, Ruble T E, Pollastro R M (2007). Unconventional shale-gas systems: the Mississippian Barnett Shale of northcentral Texas as one model for thermogenic shale-gas assessment. AAPG Bull, 91(4): 475–499

Ji L, Zhang T, Milliken K L, Qu J, Zhang X (2012). Experimental investigation of main controls to methane adsorption in clay-rich rocks. Appl Geochem, 27(12): 2533–2545

Khan M Z, Feng Q, Zhang K, Guo W (2019). Biogenic silica and organic carbon fluxes provide evidence of enhanced marine productivity in the Upper Ordovician-Lower Silurian of South China. Palaeogeogr Palaeoclimatol Palaeoecol, 534: 109278

Kosanke T H, Breyer J A, Denne R, Nelson R, Rosen R L, Aldin M, Warren A (2019). Controls on Production in the Eagle Ford: permeability, stratigraphy, diagenesis, and fractures. In: Camp, W K, Milliken K L, Taylor K, Fishman N, Hackley P C, Macquaker J H S. eds., Mudstone Diagenesis: Research Perspectives for Shale Hydrocarbon Reservoirs, Seals, and Source Rocks. AAPG Memoir 120

Li S, Meng F, Zhang X, Zhou Z, Shen B, Wei S, Zhang S (2021). Gas composition and carbon isotopic variation during shale gas desorption: implication from the Ordovician Wufeng Formation−Silurian Longmaxi Formation in west Hubei, China. J Nat Gas Sci Eng, 87: 103777

Long S, Feng D, Li F, Du W (2018). Prospect of the deep marine shale gas exploration and development in the Sichuan Basin. Nat. Gas Geosci., 29: 443−451 (in Chinese)

Longman M W, Milliken K L, Olson T M, Drake W R (2019). A comparison of silica diagenesis in the Devonian Woodford Shale (Central Basin Platform, West Texas) and Cretaceous Mowry Shale (Powder River Basin, Wyoming). In: Camp W K, Milliken K L, Taylor K, Fishman N, Hackley P C, Macquaker J H S. eds., Mudstone Diagenesis: Research Perspectives for Shale Hydrocarbon Reservoirs, Seals, and Source Rocks. AAPG Memoir 120

Loucks R G, Reed R M, Ruppel S C, Hammes U (2012). Spectrum of pore types and networks in mudrocks and a descriptive classification for matrix-related mudrock pores. AAPG Bull, 96(6): 1071–1098

Lu Z, He Z, Yu C, Ye X, Li D, Du W, Nie H (2021). Characteristics of shale gas enrichment in tectonically complex regions—a case study of the Wufeng−Longmaxi Formations of Lower Paleozoic in southeastern Sichuan Basin. Oil & Gas Geol, 42: 86−97 (in Chinese)

Ma X, Wang H, Zhou S, Shi Z, Zhang L (2021). Deep shale gas in China: geological characteristics and development strategies. Energy Rep, 7: 1903–1914

Mastalerz M, Schimmelmann A, Drobniak A, Chen Y (2013). Porosity of Devonian and Mississippian New Albany Shale across a maturation gradient: insights from organic petrology, gas adsorption, and mercury intrusion. AAPG Bull, 97(10): 1621–1643

Milliken K L, Rudnicki M, Awwiller D N, Zhang T (2013). Organic matter–hosted pore system, Marcellus Formation (Devonian), Pennsylvania. AAPG Bull, 97(2): 177–200

Nie H, Chen Q, Zhang G, Sun C, Wang P, Lu Z (2021). An overview of the characteristic of typical Wufeng–Longmaxi shale gas fields in the Sichuan Basin,. China Nat Gas Ind B, 8(3): 217–230

Nie H, Jin Z, Sun C, He Z, Liu G, Liu Q (2019a). Organic matter types of the Wufeng and Longmaxi Formations in the Sichuan Basin, south China: implications for the formation of organic matter pores. Energ Fuel, 33(9): 8076–8100

Nie H, Sun C, Liu G, Du W, He Z (2019b). Dissolution pore types of the Wufeng Formation and the Longmaxi Formation in the Sichuan Basin, south China: implications for shale gas enrichment. Mar Pet Geol, 101: 243–251

Pan L, Xiao X, Tian H, Zhou Q, Cheng P (2016). Geological models of gas in place of the Longmaxi shale in southeast Chongqing, south China. Mar Pet Geol, 73: 433–444

Qiu Z, Zou C (2020). Controlling factors on the formation and distribution of "sweet-spot areas" of marine gas shales in south China and a preliminary discussion on unconventional petroleum sedimentology. J Asian Earth Sci, 194: 103989

Ross D J K, Bustin R M (2002). Characterizing the shale gas resource potential of Devonian Mississippian strata in the Western Canada

sedimentary basin: application of an integrated formation evaluation. AAPG Bull, 86: 1921–1938

Ross D J K, Marc Bustin R (2009). The importance of shale composition and pore structure upon gas storage potential of shale gas reservoirs. Mar Pet Geol, 26(6): 916–927

Schoenherr J, Littke R, Urai J L, Kukla P A, Rawahi Z (2007). Polyphase thermal evolution in the Infra-Cambrian Ara group (South Oman salt basin) as deduced by maturity of solid reservoir bitumen. Org Geochem, 38(8): 1293–1318

Shen C, Xie J, Zhao J, Fan Y, Ren L (2021). Whole-life cycle countermeasures to improve the stimulation effect of network fracturing in deep shale gas reservoirs of the southern Sichuan Basin. Nat Gas Ind, 41: 169−177 (in Chinese)

Sun J, Xiao X, Wei Q, Cheng P, Tian H, Wu Y (2020). Gas in place and its controlling factors of the shallow Longmaxi shale in the Xishui area, Guizhou, China. J Nat Gas Sci Eng, 77: 103272

Sun J, Xiao X, Cheng P (2021a). Influence of water on shale pore heterogeneity and the implications for shale gas-bearing property — a case study of marine Longmaxi Formation shale in northern Guizhou. Mar Pet Geol, 134: 105379

Sun J, Xiao X, Wei Q, Cheng P, Tian H (2021b). Occurrence of irreducible water and its influences on gas-bearing property of gas shales from shallow Longmaxi Formation in the Xishui Area, Guizhou, southern China. Front Earth Sci, 9: 654136

Tian H, Pan L, Xiao X, Wilkins R W T, Meng Z, Huang B (2013). A preliminary study on the pore characterization of Lower Silurian black shales in the Chuandong Thrust Fold Belt, southwestern China using low pressure N_2 adsorption and FE-SEM methods. Mar Pet Geol, 48: 8–19

Wang H, Guo W, Liang F, Zhao Q (2015). Biostratigraphy characteristics and scientific meaning of the Wufeng and Longmaxi Formations black shales at well Wei 202 of the Weiyuan Shale Gas Field, Sichuan Basin. J Stratigr, 39: 289−293 (in Chinese)

Wang S J, Yang T, Zhang G S, Li D, Chen X (2012). Shale gas enrichment factors and the selection and evaluation the core area. Chin Eng Sci, 14: 94−100 (in Chinese)

Wood D, Schmit B, Riggins L, Johnson B J, Talley C (2011). Cana Woodford stimulation practices—a case history. In: North American Unconventional Gas Conference and Exhibition Articles 143960, Woodlands, Texas, USA

Xi Z, Tang S, Zhang S, Yi Y, Dang F, Ye Y (2019). Characterization of quartz in the Wufeng Formation in northwest Hunan Province, south China and its implications for reservoir quality. J Petrol Sci Eng, 179: 979–996

Xiao X M, Wei Q, Gai H F, Li T F, Wang M L, Pan L, Chen J, Tian H (2015). Main controlling factors and enrichment area evaluation of shale gas of the Lower Paleozoic marine strata in south China. Petrol Sci, 12(4): 573–586

Yang R, Jia A, He S, Hu Q, Dong T, Hou Y, Yan J (2020). Water adsorption characteristics of organic-rich Wufeng and Longmaxi Shales, Sichuan Basin (China). J Petrol Sci Eng, 193: 107387

Yang Y (2016). Application of bitumen and graptolite reflectance in the Silurian Longmaxi Shale, southeastern Sichuan Basin. Petrol Geo Experi, 38: 466−472 (in Chinese)

Zhao J, Jin Z, Jin Z, Wen X, Geng Y (2017a). Origin of authigenic quartz in organic-rich shales of the Wufeng and Longmaxi Formations in the Sichuan Basin, south China: implications for pore evolution. J Nat Gas Sci Eng, 38: 21–38

Zhao J, Shen C, Ren L, Tan X (2017b). Quantitative prediction of gas contents in different occurrence states of shale reservoirs: a case study of the Jiaoshiba Shale Gasfield in the Sichuan Basin. Natur Gas Ind, 37: 27−33 (in Chinese)